# Evaluating Central San Andreas Fault Creep in Response to the 2019 Ridgecrest Earthquake Sequence

Adam Margolis

Advisor: Dr. Mong-Han Huang

University of Maryland
Geology 394

30 November 2020

**TABLE OF CONTENTS**

## ABSTRACT

On 4 July 2019 at 10:33 am Pacific Daylight Time (PDT), the Ridgecrest earthquake sequence began with a $M_w$ 6.4 foreshock, ending a nearly 2-decade long earthquake drought (>$M_w$ 6.0) in California. Thirty-four hours later, on 5 July 2019 at 8:19 pm PDT, the $M_w$ 7.1 mainshock occurred. The sequence caused stress to be regionally redistributed. Along the central San Andreas Fault, where aseismic creep is naturally occurring, stress was slightly decreased as a result of the sequence. GPS displacement data from 11 stations were used to determine if the creep rate had decreased. The data were used to construct two timeseries (month and year) to determine if any change in the creep rate was short-term or long-term. The results show that the creep rate likely did not change on either the short-term or long-term timescales. These results suggest that there could be a theoretical critical value of stress which must be achieved to initiate a detectable change in the creep rate. This value was not exceeded from the Ridgecrest sequence, hence why there was no measurable change in creep. A Coulomb stress analysis was conducted for the central San Andreas Fault (CSAF) region to quantify the stress change associated with the sequence and to suggest a range for this critical value of stress.


## INTRODUCTION

The sequence occurred 200 km northeast of Los Angeles and caused widespread moderate shaking throughout Southern California. Figure 1 shows where the $M_w$ 7.1 mainshock epicenter was relative to the Garlock Fault and San Andreas Fault. The green line denotes the location of the central San Andreas Fault, where this study is focused.

The foreshock increased stress, locally, to initiate the mainshock on a separate nearby fault. The mainshock had a 3% chance of occurring within 7 days of the foreshock (Milner et al., 2019). It only took 34 hours.

The foreshock and mainshock occurred on separate, orthogonal faults. This is most noted in the different motion associated with each earthquake. The foreshock displayed left-lateral strike slip motion, while the mainshock displayed right-lateral strike slip motion. Most faults in California are aligned with the San Andreas Fault and, therefore, most display right-lateral strike slip motion. However, the Garlock Fault, the second longest fault in California, displays left-lateral strike slip motion. The Garlock Fault is much closer to the sequence (within 30 km) than the San Andreas Fault.

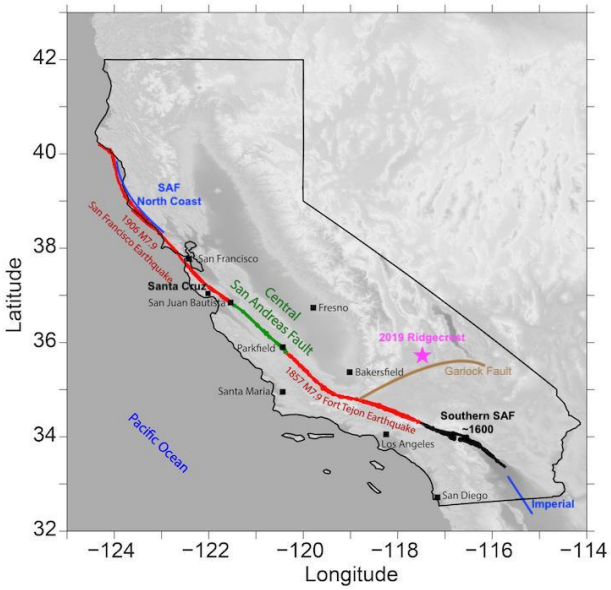


**Figure 1**: Map of California with the Ridgecrest mainshock epicenter indicated by the purple star. The Garlock Fault is shown in brown. The San Andreas Fault is shown in red, green, and black. The green section is where creep is naturally occurring and is the focus of this study. The red sections are the rupture lengths associated with two of the largest earthquakes to have been recorded in California. The blue lines are two areas that were studied by Smith and Sandwell (2003). From: Arizona State University (2018).

The two faults associated with the sequence were unmapped prior to the earthquakes, however they are located near the Little Lake Fault Zone. The zone is part of the southern end of Owens Valley and the Eastern California Shear Zone (Walker Lane) which has had large earthquakes in the past, most notably with the 1872 Owens Valley earthquake (estimated to be $M_w$ 7.4 to 7.9). Its fault scarp is easily visible today, nearly 150 years later.

When the $M_w$ 7.1 mainshock occurred, stress was regionally redistributed as displayed by the Coulomb stress map in Figure 3. Initial P-wave seismometer data as shown in Figure 2 were collected to produce Figures 2 and 3. An initial uptick on a seismogram indicates compression at that site, signifying the site physically moved away from the epicenter. Likewise, if the seismogram shows an initial downtick then it would describe extension, or decompression, was observed at that station, indicating the site physically moved towards the epicenter.

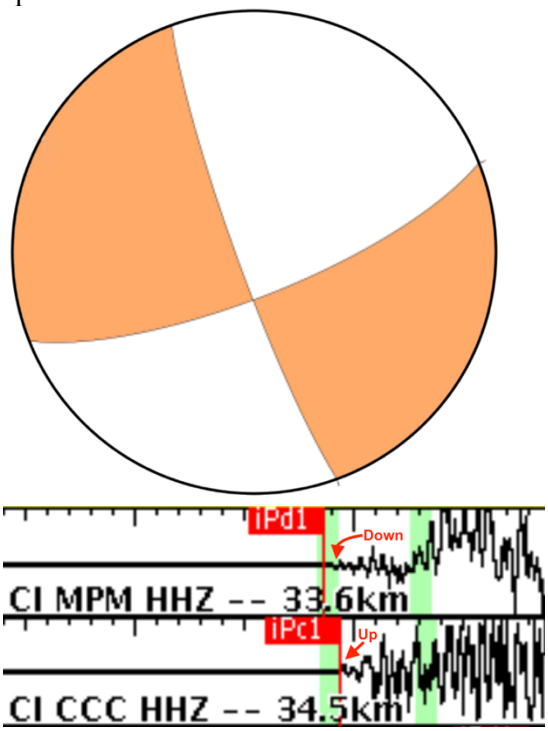


**Figure 2**: Ridgecrest Mw 7.1 mainshock focal mechanism cross section created by observing initial P-wave motions. Two seismometer stations with their distance from the epicenter noted displaying recorded seismogram P and S wave motions. The leftmost green line marks the initial P-wave and the rightmost green line marks the initial S-wave data. An uptick in initial P-wave motion indicates compression and is translated to a focal mechanism as the orange region. A downtick indicates extension and is indicated by the white region. The x-axis is time in seconds, with each vertical tick mark indicating one second. The y-axis is ground movement in millimeters. From: United States Geological Survey (2019).

For a fault that displays purely strike slip motion the four quadrants meet in the center of the focal mechanism. In Figure 2, the focal mechanism is slightly off-centered, with the intersection offset towards the southern hemisphere, implying the fault is not a pure strike slip fault. The non-uniform strike slip focal mechanism describing the Ridgecrest mainshock is consistent with a minor vertical component. This is also consistent with several field observations which revealed mean vertical displacement surface ruptures of 1.1 m (Mahmud et al., 2019).

A focal mechanism describes the 3-dimentional displacement relative to the hypocenter of an earthquake, with that being the center of the sphere. A hypocenter is the point in Earth's crust where an earthquake originated from while the epicenter is the point on the Earth's surface that is directly above the hypocenter. The focal mechanism in Figure 2 can be placed directly above the epicenter (with north orientated at the top of the circle and south at the bottom). A focal mechanism provides a visual representation of the movement of the fault planes as well as the strike, dip, and rake of that fault. The strike is the compass orientation (from 0º to 360º) of the fault. The dip is the angle the fault plane makes with the horizontal. The rake is the angle between the strike line and the fault plane. According to the USGS the fault strike, dip, and rake of the Ridgecrest mainshock are 160º, 84º, -165º respectively. Strike slip faults have a dip approaching 90º and a rake of 0º for left-lateral motion and -/+180º for right-lateral motion. For comparison, the fault associated with the Ridgecrest mainshock is classified as a right-lateral strike slip fault.

A Coulomb stress map describes the 2-dimentional stress redistribution due to displacement from an earthquake. A focal mechanism and Coulomb stress map are similar, but are describing different results. Conducting a Coulomb stress analysis can help explain where seismicity rates increased or decreased in a region, which are vital for this study (Mallman and Zoback, 2007).

My hypothesis is: *a decrease in the creep rate of the central San Andreas Fault occurred due to a decrease in stress as predicted by the Coulomb stress analysis from the 2019 Ridgecrest earthquake sequence.* In order to test this hypothesis, I used two methods: one to calculate creep rates using GPS displacement

data; and, another to quantify the stress change along the San Andreas Fault using a Coulomb stress analysis.

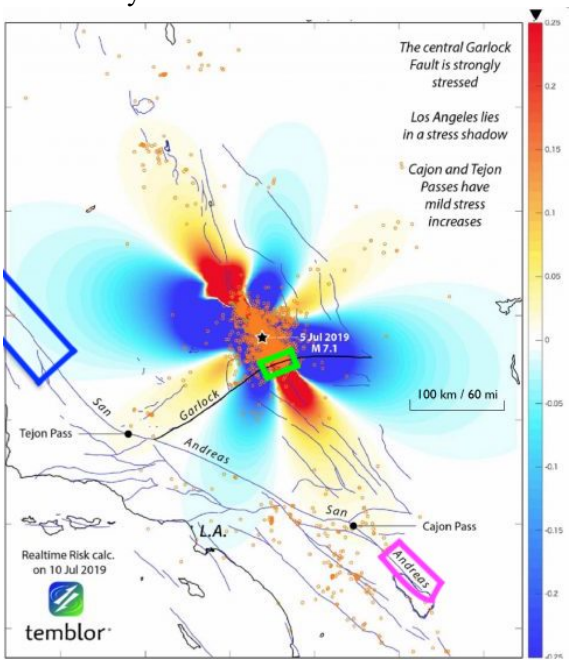


**Figure 3**: An initial Coulomb stress transfer map of the Ridgecrest Mw 7.1 mainshock, indicating where stress was increased (red/orange) and decreased (blue) in Southern California. The scale on the right is in bar. The green box is the area of study by Ross and others (2019). The purple box is the area of study by Bilham and Castillo (2020). The blue box denotes the area of this study. From: Toda and Stein, (2019).

It is estimated the Garlock Fault zone experienced a stress increase of up to 0.25 bar (region of the green box in Figure 3). The increase of stress caused a small portion (< 10 km length) of the Garlock Fault to have a maximum creep displacement of 2 cm, roughly 30 km away from the epicenter of mainshock, and less than 5 km away from the southern end of the Ridgecrest rupture during July and August 2019 (Ross et al., 2019). The results by Ross and others (2019) were found using InSAR (interferometric synthetic aperture radar) data in the Garlock Fault region. Along the southernmost section of the San Andreas Fault, up to 4.3 mm of creep was recorded using creepmeter data due to the stress redistribution associated with the 2019 Ridgecrest earthquake sequence (Bilham and Castillo, 2020). This area, adjacent to the eastern side of the Salton Sea, experienced a slight increase in stress. Similarly, the region within the blue box experienced a slight decrease in stress.

The area of study for this project is along the central section of the San Andreas Fault indicated by the blue box in Figure 3 and green line in Figure 1. Aseismic creep is naturally occurring here at a rate of 28.2 ± 0.5 mm/yr (Titus et al., 2006). Aseismic fault creep is the movement of a fault without the need of earthquakes. Creep can be a fast process as in the case of the central San Andreas Fault or it could be a slow process such as along the Hayward Fault. For comparison, the creep rate of the Hayward Fault was measured as low as 1.7 mm/yr in some places, nearly fourteen times slower than the San Andreas Fault (Shirzaei and Bürgmann, 2013).

Creep rates are not constant everywhere along a fault for a number of reasons. On a regional scale, faults cross-cut heterogenous materials, each of which fracture and behave differently under varying stress conditions. Therefore, it is important to keep in mind the rock types when studying creep rates along a fault as variations in rock type can lead to variations in creep rates. For the purposes of most studies, creep rates are calculated as an average over a large area to accommodate small variations. Another way to calculate creep rates is to focus on much smaller sites, such as a single GPS station. For this study, I focused on the CSAF as a whole, thus an average of 11 GPS stations were used to determine the overall creep rate of the region.

The most commonly accepted factors affecting creep are due to minerology, heterogenous stress conditions, and high pore fluid pressure of sediments (Harris, 2017). Each of these variables lowers the coefficient of static friction between the two blocks on either side of a fault. In the case of most Northern California faults, creep is due to the mineralogy at the surface, and often subsurface (Harris, 2017). Central San Andreas Fault creep is due to a high content of clay minerals in addition to stress inconsistences from the locked sections on both ends of the central portion of the fault.

A locked fault accumulates stress in an interseismic fashion. The locked sections of the San Andreas Fault are accumulating stress at

different rates, causing the central section to strain and creep in response. The central San Andreas Fault acts as a buffer, linking the two blocks together. This buffer helps alleviate the stress accumulated on either end of the CSAF due to the relatively low friction between the plates. The northern end of the creeping section (near Santa Cruz) builds up stress at a rate of 3.2 MPa/100yr, while the Parkfield transition builds up stress at 4.0 MPa/100yr (Smith and Sandwell, 2003). Evaluating the entire San Andreas Fault system at its most northern and southern ends produces results of 2.3 MPa/100y and 10.0 MPa/100y, respectively (Smith and Sandwell, 2003). Figure 1 shows the northern (San Andreas North Coast) and southern (Imperial) sections as the blue lines.

Clay minerals such as smectite, illite, and chlorite at a depth of 2.5 km are key factors in CSAF creep (Ikari, 2019). This was only made possible by retrieving core samples from the San Andreas Fault Observatory at Depth (SAFOD). Opened in 2002, SAFOD is a drill site located near Parkfield which can collect core samples directly from the San Andreas Fault. Additionally, talc and serpentine minerals at the surface, and to an extent the shallow subsurface, lower the shear strength of the fault allowing creep to occur at a stable rate (Harris, 2017). Serpentine and talc are metamorphic minerals which form in high pressure, low temperature conditions commonly found within subduction zones.

Roughly 30 million years ago, the entire western coast of North America was bounded by a subduction zone. The subducting Farallon Plate slid under the North American Plate, creating a volcanic arc along the west coast of the continent. Partial melting of the Farallon Plate caused felsic plutons to rise and eventually cool. The processes created enormous granite batholiths that have since uplifted to create the modern Sierra Nevada Mountains and Yosemite National Park. Soon after the Farallon Plate fully subducted, regional stress shifted and created what would eventually become the new plate boundary along the San Andreas Fault. Figure 4 describes the progression of plate motion, eventually leading to the creation of the modern San Andreas Fault. Many of the minerals found in the CSAF region formed as a result of this ancient continental collision.

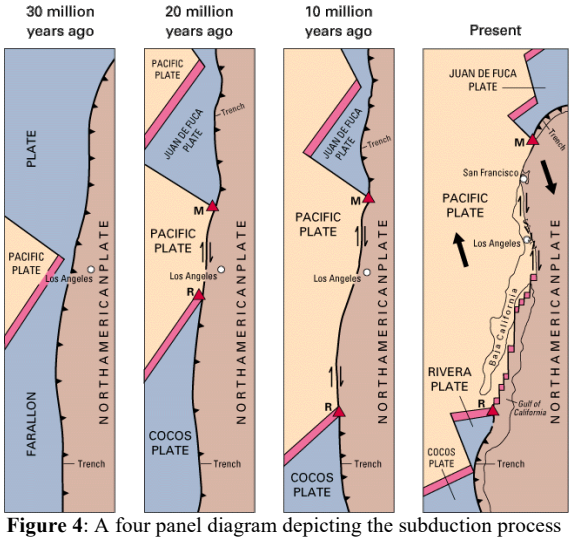


**Figure 4**: A four panel diagram depicting the subduction process of the Farallon Plate under the North American Plate at four instances in time. The Farallon Plate had jagged margins, leading to part of it subducting completely. The Juan de Fuca Plate off the northwest coast of the United States once was connected to the Cocos Plate off the western coast of Mexico. From: United States Geological Survey (1999).

Minerals from the clay group tend to crumble and fall apart under high stress conditions commonly found at plate boundaries, weathering them down into a powder, attributing to their relatively low Mohs harnesses (1 to 2.5). The powder allows the two plates to slide past one another without building up much stress. The northern and southern section of the San Andreas Fault are locked as they are continuously building up stress, possibly causing a larger earthquake than what occurred in Ridgecrest. The southern section of the fault contains igneous provinces, most notably near Joshua Tree National Park. Igneous minerals are comparatively more difficult to weather and reduce in grain size than clay minerals, allowing stress to accumulate. The most recent rupture event of the southern San Andreas Fault was estimated to be from 1440 to 1660 A.D. (McGill et al., 2002).

Similar studies of interseismic creep events due to moderate ($\geq M_w$ 6.0) earthquakes have been conducted both inside and outside of California. The 2003 $M_w$ 6.5 San Simeon Earthquake occurred roughly 100 km southwest of the CSAF. The northern part of the creeping

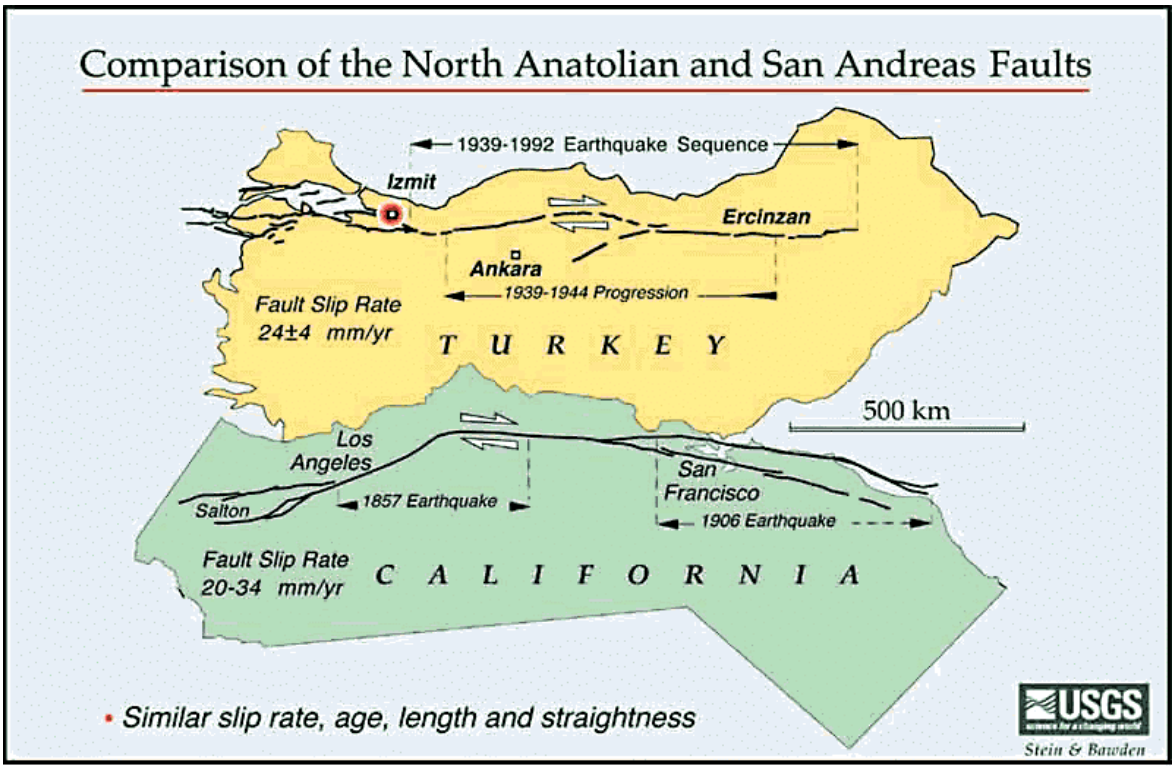


**Figure 5**: A side-by-side comparison of the San Andreas and North Anatolian Faults in California and Turkey, respectively. The faults behave similarly; having comparable slip rates, lengths, and size of earthquakes as well as being located near major cities. The brown and red dot marks the epicenter of the 1999 Izmit Earthquake. From: Kalkan

section was in a stress shadow zone, while the southern creeping section saw an increase in stress. The creeping section that was within the stress shadow zone experienced a decrease in creep rates from 90 days before to 90 days after the earthquake (Meng et al., 2013). The study also found where stress increased along the creeping section, seismicity rates also increased. A few things to keep in mind with this study. The earthquake magnitude was smaller than the 2019 Ridgecrest earthquake sequence, however the epicenter was much closer to the fault. Also, the faulting for both events is different. The San Simeon event was from a blind thrust fault, while the Ridgecrest earthquakes were from strike slip faults. Thus, their Coulomb stress models would appear different.

Comparable studies have been completed on the North Anatolian Fault in Turkey. In many ways, the North Anatolian Fault is similar to the San Andreas Fault (Figure 5). They both display right-lateral strike slip motion and they both define a plate boundary. The North Anatolian Fault is situated between the Eurasian and Anatolia Plates.

One study, by Hussain and others (2016), was conducted along the 140 km rupture length of the $M_w$ 7.6 1999 Izmit Earthquake using data from InSAR and GPS receivers. Prior to the earthquake during the preseismic period there was little to no displacement or creep, indicating the fault was locked and accumulating stress. Immediately after the initial displacement from the earthquake, creep was induced in the North Anatolian Fault at a rate of $2.9 \pm 0.4$ mm/d, before leveling off at a roughly constant rate of 5 mm/yr after five years (Hussain et al., 2016). The study went on to compare GPS data up to 2012 and creep associated with the 1999 Izmit Earthquake was still measurable. The North Anatolian Fault creeps due to clay and mica rich fault gouge, acting as a lubricant to reduce friction (Kaduri et al., 2017). The information provided by Hussain and others (2016) indicates that the highest creep rates are likely to occur in the time closest to the initial rupture of an earthquake. It is in this time frame, in the days or weeks after a large earthquake,

that creep is most prevalent and most easily measurable.

## PROCEDURE

The study area for this project is in a stress shadow zone which experienced a decrease in stress of up to 0.05 bar (Figure 3). There should be less stress to drive creep motion in the central San Andreas Fault region after the 2019 Ridgecrest earthquake sequence. Therefore, a decrease in the creep rate should also occur along the San Andreas Fault from Cholome to San Juan Bautista.

I evaluated CSAF creep rates using GPS displacement data provided by the United States Geological Survey (USGS) and the Nevada Geodetic Laboratory (NGL). The two organizations use the same GPS stations. However, they process their data slightly differently. Therefore, I compared the results from both organizations to observe if any biases exist and to verify if the data were consistent with one another.

Two timeseries were created to observe the trends of the data. The first was a month before compared to a month after (30 days). These results were conclusive and used in this study. The second timeseries compared the data from a year before to a year after (365 days). These results were also conclusive and contributed to this study. Lastly, a Coulomb stress analysis was conducted for the central San Andreas Fault region. This was used to determine the quantity of the stress decrease along the CSAF.

### *I. GPS*

For this study, five stations were selected on the Pacific Plate and six on the North American Plate. The data have been recorded in real time at a rate of twenty times per second. Each station records both vertical and horizontal displacement data. However, only horizontal displacement is critical in this study as creep motion is strictly horizontal in the CSAF region. Horizontal GPS data were downloaded from eleven stations that are within close proximity (± 20 km) of the CSAF zone. The proximity of the stations must be close in order to compare creep rates accurately. This is to minimize the chance of natural plate motion being recorded as it is not associated with creep or fault movement. Additional stations were considered, however, some were missing data within one or both of the timeseries.

Another reason for not including some GPS stations is that their residuals were too irregular (due to moisture). The residuals consist of taking the calculated creep rate equation from the Excel plot and plugging in the decimal day for $x$ where the displacement, $y$, is calculated. The net difference between the recorded and calculated displacement $y$ values are plotted and observed for any discrepancies. An accepted seasonal variation would have a smooth, repeating curve (similar to a sine wave). Figure 6 shows a residual plot from the LAND station.

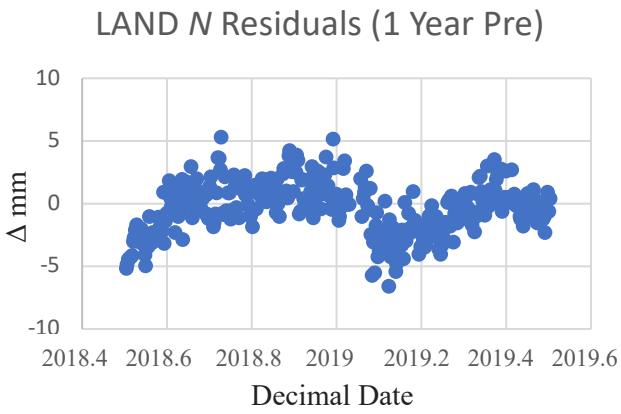


**Figure 6**: Residual plot from the LAND GPS station using its USGS north (*N*) data recorded from 3 July 2018 to 3 July 2019. The plot was created by taking the measured value and subtracting the calculated value of displacement. Those net values are plotted above. Seasonal variations (moister) create a repeating function.

The GPS stations are above ground and stand on a three or four post structure with a central pylon drilled into the bedrock. This is to minimize station movement due to wind, erosion, or human or animal activity that could otherwise rattle the station. The actual GPS receiver is located at the top, roughly 2 to 3 m above the ground, and is in the shape of half a sphere which is often painted grey. Figure 7 provides a picture of what the stations look like in the field. Due to the remote locations of most stations, many are solar powered.

### *Ia. GPS Processing – USGS*

The USGS GPS data were processed on a Macbook Pro. I visited the *GPS Data* webpage under the *Earthquake Hazards Program* section on the USGS website. There is an interactive map marking the location of all twenty-nine networks across the United States. It also lists them below the map. First, I selected the *CentralCalifornia* Network. The map of all the GPS stations in the network will then appear.

**Figure 7**: A photo of the WHYT GPS station in Southern California with myself as a scale. USGS has thousands of GPS stations spread across the state just like this one. The half-domed structure at the top is the GPS receiver, while the angled posts are meant for support. The station has a central pylon drilled into the bedrock for stability and to prevent inaccurate readings from erosion, wind, or human or animal activity which could otherwise rattle the station. Note the solar panel and radio transmitter in the background (left). The radio transmitter sends data via satellite to the USGS office in Menlo Park, California for processing.

On the interactive map, hand picking stations is a relatively straightforward process given the guidelines outline on the previous page. The LAND station, for example, is one of the stations that satisfies the parameters.

To start processing the data in Excel, the raw data must be download from that station. I found the LAND station on the interactive map by moving the cursor on the blue triangles, indicating the station is currently online. The name of the station will appear next to the cursor. Once the LAND station is found, I clicked the blue triangle to open its webpage. Next, I found the *Downloads* section. Under *Raw Data*, I clicked on *All*. This prompted a file download. Then I right clicked the downloaded file, named *land.rneu*, and selected *Open with* and clicked *Other*. A popup screen appeared with a list of applications where the file could be opened and viewed. From the dropdown menu, I selected *All Applications*. Then I double clicked on Excel. The data loaded into several columns. USGS does not label columns, so Table 1 shows how the data are organized.

The downloaded spreadsheet provides the daily average displacements from a fixed reference frame (in millimeters) in chronological order. It contains data from when the station was originally placed online, therefore the data relevant to this study (3 July 2018 to 5 July 2020) must be searched for within the spreadsheet. USGS records data in terms of daily average displacement magnitudes, in millimeters, from unit vectors orientated in the north (*N*), east (*E*), and up (*U*) directions. The up direction is the vertical displacement measurement. As mentioned previously, the up data can be ignored as CSAF creep is strictly horizontal. According to the USGS, the horizontal uncertainty for calculating velocities with GPS data is ± 2.5 mm/yr (2σ).

When the displacement plots are created, in the year prior, there are two data points that must be removed. These data points are showing displacements of over 1000 mm/d and are due to regular system updates or readjustments. These exaggerated data can be seen easily on the plot and can be removed by deleting the row associated with them. They occur on 24 and 25 April 2019. This is a systematic error as the exaggerated data can be seen on all observed USGS GPS stations.

### *Ib. GPS Processing - NGL*

The NGL GPS data are processed in a similar way. First, I visited the *Nevada Geodetic Laboratory GPS Networks Map* homepage. I then use the map feature to find the central San Andreas Fault region. Then I located the LAND station. GPS station sites are marked by red or blue squares. When one is clicked on the map, several plots of that GPS station will be shown. Clicking any of the plots will open the webpage for that specific GPS station. Under *Time Series*

| | A | B | C | D | E | F | G | H | I |
|---|---|---|---|---|---|---|---|---|---|
| 1 | Date | Decimal | N | E | U | | N ± | E ± | U ± |
| 2 | 19990826 | 1999.6502 | -392.1 | 317.3 | -1 | rrr | 3.1 | 3.3 | 10.9 |
| 3 | 19990827 | 1999.6529 | -389.8 | 317.8 | -18.7 | rrr | 2.9 | 3.4 | 10.6 |
| 4 | 19990828 | 1999.6557 | -389 | 321.2 | -12.5 | rrr | 2.9 | 3.5 | 10.3 |
| 5 | 19990829 | 1999.6584 | -389.1 | 320.7 | -13.4 | rrr | 2.9 | 3.5 | 10.5 |
| 6 | 19990830 | 1999.6611 | -388.8 | 319.7 | -13.8 | rrr | 3 | 3.4 | 10.5 |
| 7 | 19990831 | 1999.6639 | -388.1 | 317.7 | -17.7 | rrr | 3 | 3.5 | 10.3 |

**Table 1**: Screenshot of USGS GPS data provided by the LAND station in Excel from 26 August 1999 to 31 August 1999. The yellow row (row 1) was manually entered into the spreadsheet to label the columns. The data are recorded as daily average displacements and are organized by the date the data were recorded. Decimal is the decimal date of the day the data were recorded. *N*, *E*, *U* are the north, east, and up displacement data, respectively in millimeters. A negative number indicates displacement in the opposite direction (e.g. -392.1 for *N* indicates 392.1 in the south, *S*, direction). *N* ±, *E* ±, and *U* ±, are the uncertainties of *N*, *E*, and *U*, respectively, to 2σ. *rrr* is a column break and used for organization purposes.

*Data*, I clicked *env* (east north vertical) just to the right of *NA*. The first column (beginning with IGS14) is simply the reference frame. The USGS GPS data uses stable North America as its reference frame, thus the data from NGL should also use the same reference frame.

Once *env* is clicked, a webpage of data is listed from when the station first went online. Therefore, I manually searched for the data which are relevant to this study (3 July 2018 to 5 July 2020). NGL does label its columns, unlike USGS. To make processing the data easier, I saved the webpage as a *TextEdit* file. I then opened the *TextEdit* file and removed the data which were not relevant to this study. The north and east data are labeled as *_east(m)* and *_north(m)*, respectively. Note, the daily average displacements are in terms of meters, thus each element must be multiplied by 1000 to convert units from meters to millimeters.

The *yyy.yyy* (decimal year) column along with the converted east and north

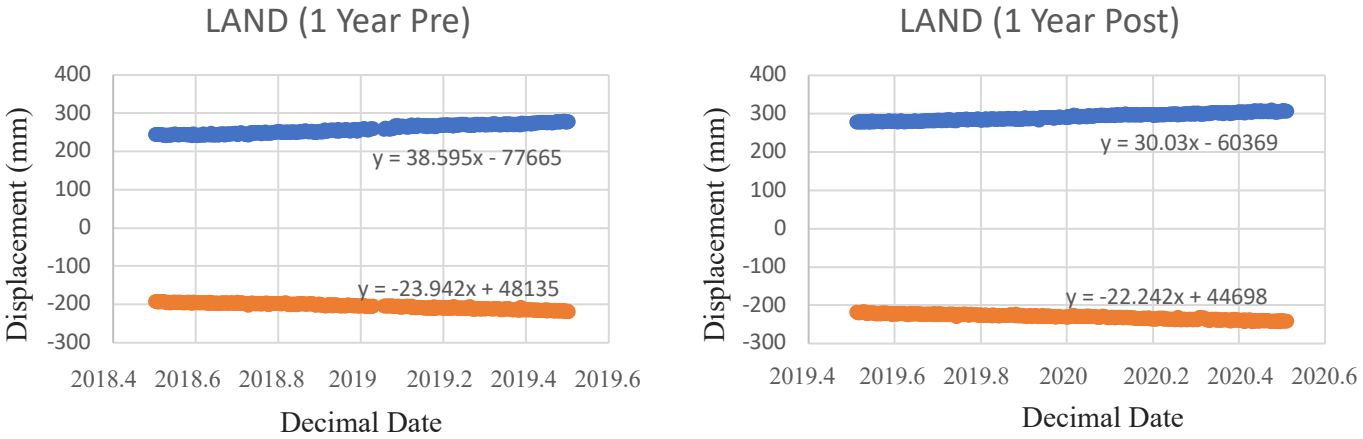


**Figure 8:** Two average daily displacement (mm) verses time (decimal date) plots recorded from the LAND station on the Pacific Plate. The pre-Ridgecrest plot (left) was created using USGS data from 3 July 2018 to 3 July 2019. The post-Ridgecrest plot (right) was created using data from 6 July 2019 to 5 July 2020. The blue and orange curves are the north and east displacement data, respectively. The slope of these curves are the calculated vector magnitudes (creep rates in mm/yr) for that given orientation. For example, -23.942 mm/yr is the calculated creep rate and magnitude for a vector orientated in the east direction in the year prior to the Ridgecrest earthquake sequence at the LAND station. The calculated slopes for the blue and orange curves can be used in Equation 1 to determine the magnitude of the resultant vector. This is equal to the overall creep rate recorded at a particular station. Equation 2 can be used to determine the direction of the creep rate.

displacement values can be copied into Excel where they can be plotted on a time verses displacement curve. The slope of the curve is the calculated creep rate at that particular GPS station. According to NGL, the horizontal uncertainty for GPS data is ± 2 mm/yr (2σ). The NGL data is from Blewitt and others (2018).

### *Ic. GPS Calculations*

By combining the north and east magnitudes to find the resultant vector, the creep rate can be calculated as well as its direction of motion. Equation 1 describes mathematically how the magnitude of the resultant vector can be calculated. *N* and *E* are the slopes of the north and east displacement curves (Figure 8). The value of *N* and *E* can be plugged into Equation 1 to determine the magnitude of the creep rate. *R* is the resultant vector which measures the total creep rate based on the N and E unit vector values.

$$(\boldsymbol{N})^2 + (\boldsymbol{E})^2 = (\boldsymbol{R})^2$$

**Equation 1**

$$\boldsymbol{\theta} = \arctan\left(\frac{\boldsymbol{E}}{\boldsymbol{N}}\right)$$

**Equation 2**

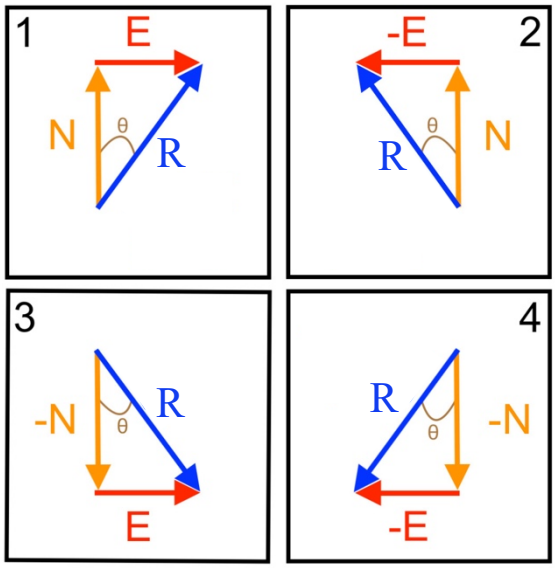


**Figure 9**: Visual representation of north (*N*) and east (*E*) GPS data in terms of vectors. The orange, red, and blue vectors represent the north, east, and resultant vectors, respectively. GPS data are recorded in terms of north and east displacements. The north and east magnitudes are the slopes of the respective displacement curves. The resultant vector (*R*) shows both the direction of the displacement, $\theta$, and its magnitude.

Equation 2 describes how the direction of the resultant vector can be calculated with respect to the north unit vector as shown in panel 1 of Figure 9. Given the north and east magnitudes, the orientation of the resultant vector, $\theta$, can be calculated.

If the *N* and *E* values for each station are known, they can be plugged into a GMT script where *R* and $\theta$ are automatically calculated and plotted on a 2D map. The code for this can be found in Appendix I. The background creep can be plotted for the year prior and compared to the net difference. Figure 11 (1a. and 1b.) describes the background creep rates and the difference in creep rates in the year and month timeseries. One of the eleven stations, P249, is kept as a reference station. Therefore, any variations that may exist can be seen more clearly among the other ten GPS stations. P249 is chosen because in the year timeseries, it recorded an average creep rate compared to the other GPS stations in this study. It also recorded an average creep rate change in the month timeseries in both magnitude and direction.

Data were downloaded from 3 July 2018 to 5 July 2020. The dates of the earthquake (4 and 5 July 2019) were not included in the data collection process to prevent displacement from the 2019 Ridgecrest earthquake sequence skewing the results. The largest displacement occurs during an earthquake. Therefore, if the CSAF region moved as a result of the Ridgecrest earthquake sequence, the creep rate calculations would be inaccurate if the sequence dates were included. The year timeseries contains data from the pre-Ridgecrest (3 July 2018 to 3 July 2019) and post-Ridgecrest (6 July 2019 to 5 July 2020) periods. Note that 2020 is a leap year, therefore the total number of days (365) are the same within the defined post-Ridgecrest year timeseries compared to the pre-Ridgecrest year timeseries. The month time series contains data from the pre-Ridgecrest (3 June 2019 to 3 July 2019) and the post-Ridgecrest (6 July 2019 to 5 August 2019) periods. The data recorded during the Ridgecrest (4 and 5 July 2019) earthquake sequence were removed.

*Id. GPS Results*

The top image in Figure 10 describes the normal plate motion across the central San Andreas Fault. The bottom image shows what is expected if the creep rate is decreased. The net difference in the creep rate should show an acceleration in the opposite direction of plate motion, suggesting there is an overall decrease in the creep rate.

The creep rate in the year prior to the Ridgecrest earthquake sequence (or the normal background creep) was calculated with USGS and NGL data at 30.5 ± 2.5 mm/yr (2σ) and 33.5 ± 2 mm/yr (2σ), respectively. The USGS calculation is within the calculated value of 28.2 ± 0.5 mm/yr from Titus and others (2006). Additionally, the NGL calculation is also reasonable.

Observing the maps in Figure 11, the background calculated creep rate (row 1) is as expected. The vectors are pointing in relatively the same direction. However, their individual magnitudes are different. More displacement is observed on the Pacific Plate than the North American Plate, thus the overall net motion is right-lateral strike slip. The plots on the left (column a) show the creep rate magnitudes and directions relative to stable North America (NA). The plots on right (column b) show the data relative to GPS station P249. P249 is located on the North American Plate and is circled in blue in Figure 11. The results of the eleven GPS stations are shown in Figure 11.

Note that if a decrease in the creep rate occurred, then the resultant vectors should point in the opposite direction of plate motion. On the month timescale (row 3 of Figure 11), there was a net acceleration change both in direction and in magnitude among most stations. This can be seen especially in row 3, column a. However, the net resultant vectors are nearly orthogonal to the San Andreas Fault and not a complete 180º direction from the plate motion. This result implies a decrease in the creep rate was not measurable. One possibility to the orthogonal acceleration are landslides. When the earthquake happened, moderate shaking occurred along the

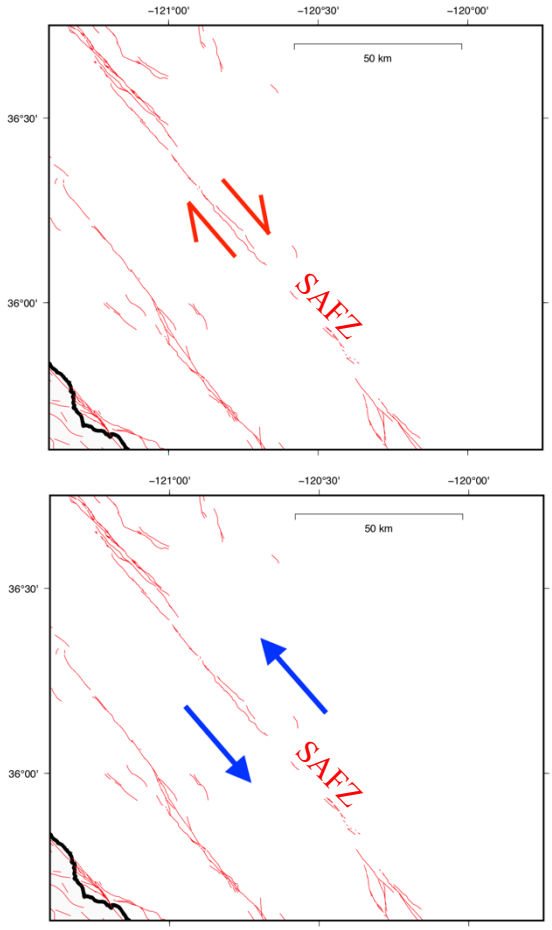


**Figure 10**: TOP: San Andreas Fault zone (SAFZ) displaying normal background right-lateral strike slip motion. BOTTOM: If a decrease in the creep rate occurred, the GPS vectors should show an acceleration of creep in the opposite direction of plate motion. This result would imply the overall net difference is a decrease in the creep rate.

central San Andreas Fault region. Some of the GPS stations are located on the peak of a hill. The slopes of the hill may have had minor landslides in the days immediately after the earthquake, causing the peak to move slightly. Figure 12 shows the LAND station on top a hill on the Pacific Plate. The orange vector is showing the calculated net displacement, pointing downslope.

However, some GPS stations are not located on a peak. For example, the P283 station is located in a moderate rolling hills region which contains more gentle slopes. While landsides from the earthquake are possible, it is less likely for them to occur on smoother terrain.

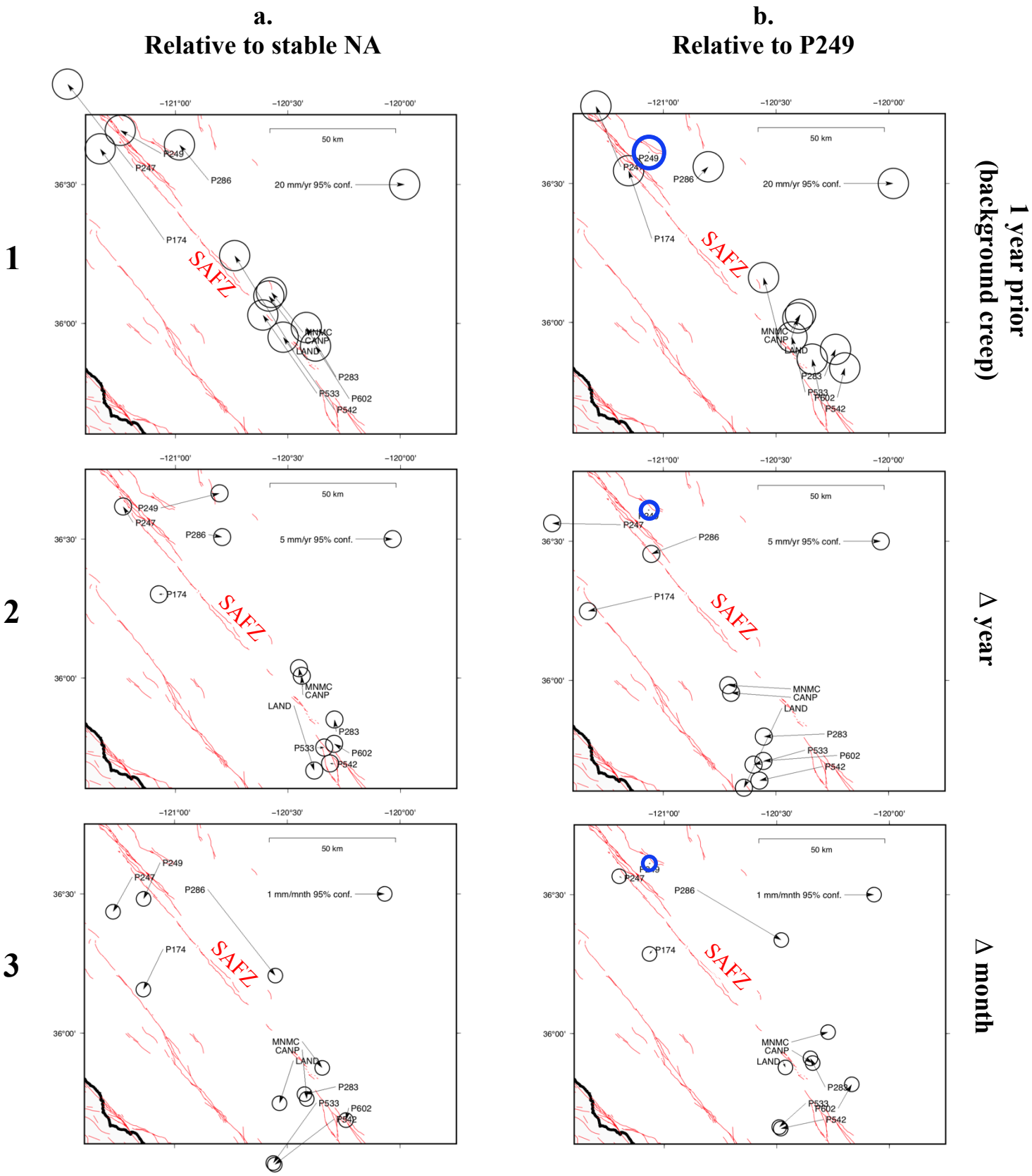


**Figure 11:** 6 GMT plots of eleven GPS stations, using USGS data, along the central San Andreas Fault zone (SAFZ) with their creep rate calculations shown as resultant vectors. The length of the vector is the magnitude of the creep rate as calculated at that specific GPS station. The circle at the arrow tip is the confidence interval to 95%. The GPS station is located at the beginning of the arrow, with its name noted. Column a. shows the creep rates relative to stable North America (NA). Column b. shows the creep rates relative to station P249 (blue circle). Row 1 is 1 year prior to the 2019 Ridgecrest earthquake sequence or the normal background creep. Row 2 is the net change in the year before to the year after the Ridgecrest event. Row 3 shows the net change in the month before to the month after 2019 Ridgecrest earthquake sequence. The script used to create these plots can be found in Appendix I.


**Figure 12:** Google Earth image of the LAND station on top of a small peak, overlooking the San Andreas Fault zone (in red). The orange vector is representing the direction in which the LAND station calculated orthogonal motion with respect to the San Andreas Fault in the month timeseries. The steep terrain in the foreground caused some creep rate measurements to be difficult to determine due to minor landslides in part because of the moderate shaking from the 2019 Ridgecrest earthquake sequence.

Another reasonable explanation for the orthogonal motion could be due to the reference frame. If the reference frame moved during the timeseries, all the GPS stations would be offset by the same amount. In Figure 11, panel 3a., most GPS stations recorded similar magnitudes in addition to similar directions. For example, stations P249, P247, and CANP have similar magnitudes and directions, which would explain the reference frame of stable North America had moved.

The net average magnitude change for all eleven stations in the month timeseries using USGS and NGL data was -7.01 ± 2.5 mm/yr (2σ) and 54.41 ± 2 mm/yr (2σ), respectively. The large value from the NGL results further suggests that the reference frame moved within the timeseries, skewing the results. There are three conclusions to draw from the results. The change in the creep rate was low enough that it was not detected. It could also imply the creep rate did not differ between the timeseries. Or it could also suggest the reference frame or landslides (or a combination of both) caused the calculated creep rates to not be as accurate.

Comparing the net year results (year before Ridgecrest to the year after), the change in the creep rate was calculated at -0.32 ± 2.5 mm/yr (2σ) (USGS) and -1.69 ± 2 mm/yr (2σ) (NGL). These results suggest the creep rate did not decrease in the year after the 2019 Ridgecrest earthquake sequence. The calculated value is lower than the uncertainty, thus any change that might have occurred was not large enough to be resolved by my methods.

Most of the stations recorded very little change in motion during this timeseries. Two stations recorded noticeable change: P249 and LAND. LAND recorded a decrease in the creep rate, but because the decrease is not seen at other GPS stations, it is likely due to erosion or landslides as previously discussed.

Appendix II shows the organized data in an Excel spreadsheet for reference.

### *Ie. GPS Uncertainties*

There are uncertainties involving GPS data which should be addressed. The GPS receivers use at least four out of the twenty-four available GPS satellites at any given time to

triangulate its position. The satellites orbit at roughly 24,000 km above the surface of Earth and each satellite orbits the planet twice, daily. All GPS satellites broadcast two radio frequencies that includes precise information about the time and the satellite's position. The GPS receiver on the ground can compare the information in the signal to its own internal clock to determining its position on Earth. The distance from the satellite is calculated by noting the time it takes for the signal to be sent from the satellite to the GPS receiver.

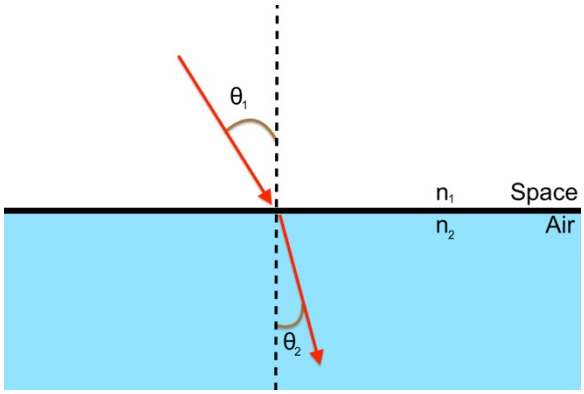


**Figure 13**: Visual representation of Snell's Law as light passes through one medium to another of different densities. Refraction occurs to radio signals due to variable atmospheric density. *n* is the index of refraction of a material, *θ* is the angle of incidence. The normal (dotted line) is perpendicular to the medium interface.

The radio signal is affected by Snell's law in Figure 13 and better described by Equation 3. The velocity of electromagnetic radiation, like radio, slows down as it travels through mediums of higher densities such as traveling through space and then through Earth's atmosphere. The radio waves are refracted and slow down causing the calculated distances to be slightly higher than they really are. The index of refraction, *n*, for a given medium is based on the density of that material. The index of refraction for air at sea level is 1.003 and in the vacuum of space it is defined as 1.000. *θ* is the angle of incidence. It is defined as the angle between the incoming ray and the normal.

$$(n_1)\sin\theta_1 = (n_2)\sin\theta_2$$

**Equation 3**

Micrometeorites and space debris are another topic to consider. This is likely less of an issue for GPS satellites as they orbit at high altitudes above the surface of the Earth. However, they are not exempt from being hit by impacts that could otherwise move their positions or cause them to fail entirely.

Most GPS stations are solar powered due to their remote locations. However, a few within the Central California network are powered by the local electrical grid, meaning they are prone to being offline during blackouts and power surges. If a station was without power, it would not be taking measurements and would produce inaccurate daily displacement averages. This did occur to several stations, making them ineligible for use in this study.

During the fire season in late summer and early fall, intentional power outages are a common practice in rural California. Dry brush, warm temperatures, and the famous Santa Ana winds are a recipe for disaster. Because the central San Andreas Fault is located in a remote region, the vast majority of stations are not powered by the local electrical grid. However, this does not mean they are invincible. GPS stations do have occasional electrical failures even if the station is solar powered. An electrical failure could put a station out of commission until it is manually fixed by a technician.

As mentioned briefly, GPS stations require occasional system readjustments to insure they are calculating displacements correctly. When this occurs, the GPS data are exaggerated and can cause the data to be skewed. This is easily fixed by manually removing the extraneous data in Excel. The plot will become smoother and will not have a single large peak or series of peaks. Any displacement data that were recorded exceeding 1000 mm on any given day is most certainty due to a system readjustment. In the case of the USGS and NGL data, only the USGS displays two extraneous data points on 24 and 25 April 2019.

One thousand millimeters of displacement can occur in a single day if attributed to a nearby earthquake. An earthquake with ≥ 1000 mm of displacement has not occurred along the central San Andreas Fault since GPS stations began to be placed in the

region in the late 1990s. The last major earthquake to occur along the central section of the San Andreas Fault was a $M_w$ 6.0 on 28 September 2004. The epicenter of this earthquake was near Parkfield and caused a maximum displacement of 0.45 m, or 450 mm (Kim and Dreger, 2008). This earthquake is one of a series of similar magnitude earthquakes that occur regularly in this region every 12 to 34 years. In the early 1990s it was wrongfully predicted that the 2004 event would occur in 1993, given the regional seismic history of past earthquakes.

To account for these issues, the horizontal GPS data provided by the USGS and NGL carries an uncertainty of ± 2.5 mm (2σ) and ± 2 mm (2σ), respectively.

### *II. Coulomb Stress Analysis*

A Coulomb stress analysis is the backbone for this study. Figure 3 was published several days after the 2019 Ridgecrest earthquake sequence. It provides a visual representation of where stress was increased and decreased, regionally. However, this map does not show the entirety of the central San Andreas Fault system. As seen in Meng and others (2013), some parts of the creeping section of the San Andreas Fault behave differently due to negative or positive stress inputs. Figure 3 provides a limited picture of the Ridgecrest stress redistribution along the San Andreas Fault region. Therefore, it is vital to conduct my own analysis and compare it to the GPS results.

Conducting a Coulomb stress analysis requires an understanding of how a fault can redistribute stress and if it is regionalized or localized. Think of a simple strike slip fault that had an earthquake. Some material one side of the fault moved in the opposite direction of the other. At the end of the rupture, this material bunches up and compresses. This occurs in the direction of motion. Likewise, material is stretched or thinned out on the other end of the rupture. This bunching up of material increases stress while the thinning out of material decreases stress. Depending on the magnitude of the earthquake, hypocenter depth, and fault orientation this stress transfer can be regional or local.

Coulomb theory describes how a stress increase from one earthquake can transfer to another nearby fault, leading it closer to failure. This is what occurred during the 2019 Ridgecrest earthquake sequence. A stress increase from the foreshock caused the much larger mainshock to occur on another nearby fault. Many seismologists were concerned that the sequence could have initiated an earthquake on the Garlock Fault (roughly 20 km away from the epicenter), eventually brining the San Andreas Fault closer to failure. An "unzip" event is not impossible, but it is rare. The closest section of the San Andreas Fault to Ridgecrest has not ruptured since the 1857 Fort Tejon earthquake.

Mathematically, a Coulomb stress transfer (or stress change) is calculated using equation 4. Coulomb stress change, $\Delta CFS$ describes the change in stress of a given point after a seismic event. A positive value indicates an increase in stress and the point is closer to failure. A negative value describes a decrease in stress and the point is brought father away from failure. The units of $\Delta CFS$ is in bar. $\Delta\tau$ is the change in shear stress. The coefficient of friction of a fault is described as $\boldsymbol{\mu}'$. The change in normal stress of a given point is denoted as $\Delta\sigma_n$.

$$\mathbf{\Delta CFS = \Delta\tau + (\mu' \Delta\sigma_n)}$$

**Equation 4**

### *IIa. Coulomb Processing*

The data were processed using the Coulomb 3 Matlab plugin, available for free download from the USGS. The Coulomb stress transfer map in the top image of Figure 14 was created using the Coulomb stress analysis feature in Coulomb 3. The data were provided by the USGS. It can be found on the *M 7.1 – 2019 Ridgecrest Earthquake Sequence* webpage. On the left-hand side, I clicked *Finite Fault*. Then I scrolled down until a drop-down menu named *Downloads* appeared. I then clicked the kb file under *Coulomb Input File* to initiate a download. Once downloaded, the file may need to be edited to have a *.inr* extension.

The downloaded *.inr* file from the Ridgecrest event needs to be saved within the *imput_file* subfolder in the *coulomb34_2* mainfolder. The *coulomb34_2* folder must be in the directory or the plugin will not work. On Matlab, in the command window, I typed *Coulomb* and hit enter to open the plugin.

A blank window appeared with a clickable user window at the top. I clicked *Input* and then clicked *Open existing input file*. Under the *input_files* folder, I found the file which I had saved from the Ridgecrest event with the *.inr* extension. I then opened the file and waited for it to load.

If done correctly, a diagonal line of various colors will appear in the center of a grid. The diagonal line represents the strike of the fault which the mainshock occurred on. It does not represent the length of the rupture. The study area must be enlarged to encompass the entire central San Andreas Fault. To do this, I right clicked on any of the numbers on the axes. I selected the *change study area* option and then changed the minimum value for the longitude to -121.78 before I clicked *OK*.

Back on the main popup window with the gridlines, I clicked *Functions* on the top of the window. Then I found *Stress* and clicked *Coulomb stress change*. A smaller popup window appeared named *Stress control panel*. I made the color saturation 0.1 bar at 1.0 bar intervals. I also changed the depth to 5.0 km before I clicked *Calc. & View*. Changing the depth to 5.0 km implies the Coulomb stress map will describe the stress at a 5.0 km depth from the surface.

Once it loaded, a Coulomb stress map will be displayed from the 2019 Ridgecrest earthquake mainshock ($M_w$ 7.1). On the Stress control panel, in the bottom left, I clicked *Cross Section*. A smaller pop up window appeared where I could input two coordinates which corresponded to point A and B on the map. A straight line would connect the two points where a cross section would be calculated to show the stress change at depth. For this study, it was most useful to have a cross section aligned with the strike of the CSAF. Therefore, I used -121.5 and 36.81 for the longitude and latitude of point A, respectively. I also used -120.2 and 35.7 for the longitude and latitude for point B, respectively. This roughly covers the entire central San Andreas Fault where the change in stress would be calculated along the fault plane.

To save the images, I clicked on *File* and then *Save As*. I selected the format to be an EPS file (.eps) as it is a higher resolution image. Once saved, I opened the file using Preview where I added lines of the San Andreas Fault (pink) and Garlock Fault (black) along with some cities. The blue line connecting points A and B is showing the cross section in map view.

### *IIb. Coulomb Results*

The results of the Coulomb stress analysis show that the stress did decrease along the entire central San Andreas Fault. The maximum amount of stress decrease along the CSAF was calculated to be 0.02 bar near Parkfield (point B in Figure 14). The lowest amount of stress decrease was close to 0 bar near San Juan Bautista (point A).

Point B in Figure 14 is closer to the Ridgecrest mainshock epicenter and therefore it experienced a larger decrease in stress than point A, which experienced close to no change in stress. The bottom image in Figure 14 describes heterogenous stress conditions, horizontally along the central section of the San Andreas Fault. Interestingly, for any given vertical line along the central San Andreas Fault, stress was homogenous.

## Discussion

The 2019 Ridgecrest earthquake sequence reminded Californians that large earthquakes can still occur in the state. The location of the sequence was far enough away from major population centers such as Los Angeles and Las Vegas to not cause any widespread significant damage.

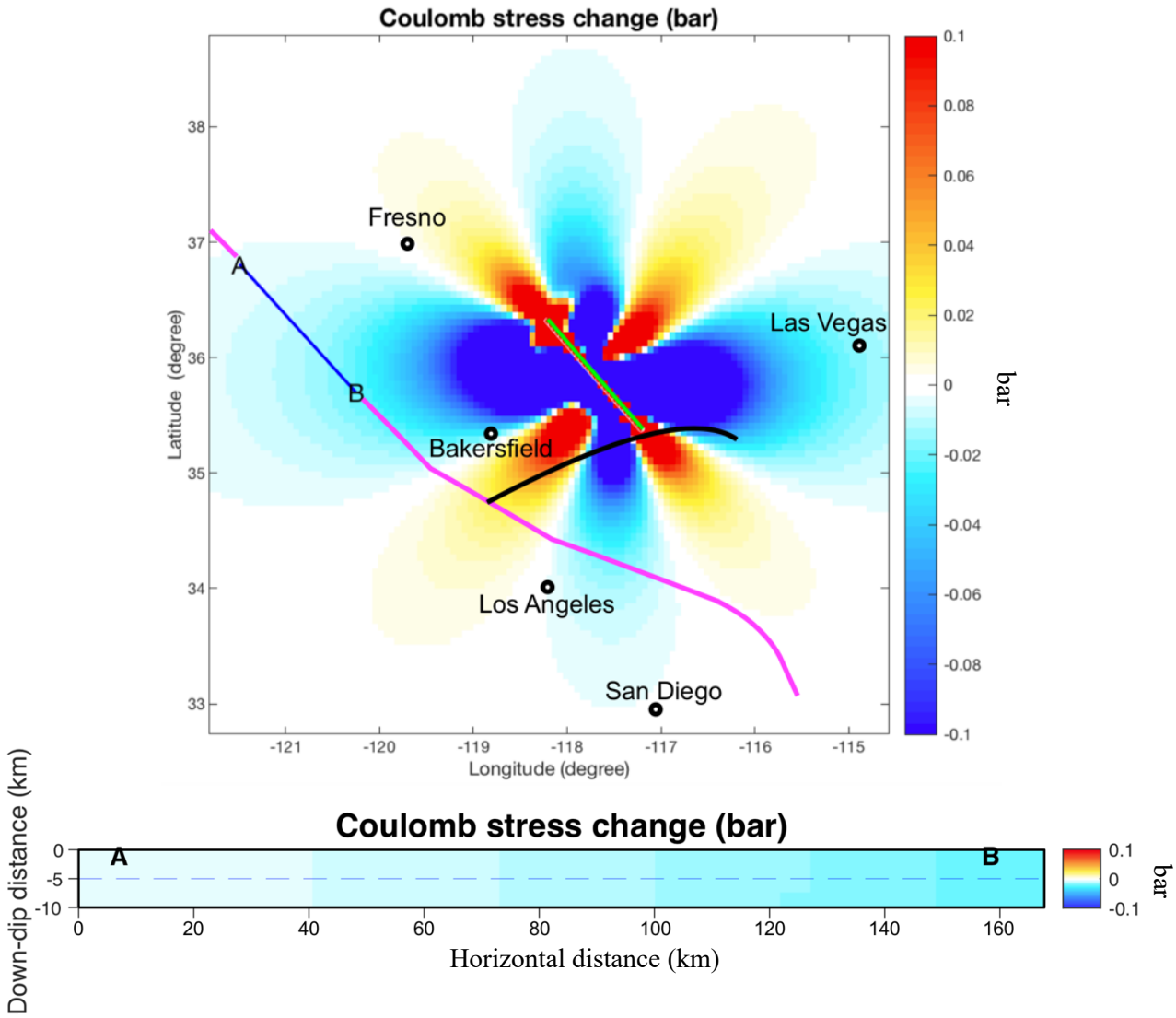


**Figure 14:** TOP - Visual representation of the Coulomb stress analysis of the Ridgecrest mainshock. The color scale on the right is in bar. The pink line is the approximate location of the San Andreas Fault. The blue line is the creeping section of the San Andreas Fault and is the line from which the cross section is calculated (bottom). The black line is the Garlock Fault. The green line is the strike of the fault associated with the Ridgecrest mainshock. BOTTOM - Visual representation the Coulomb stress cross section analysis for the central San Andreas Fault. The flat plane is the San Andreas Fault plane, where A is the northernmost point and B is the southernmost point of the central section of the fault. The color scale on the right is in bar. The dotted line is 5 km in depth, for which the Coulomb stress analysis is presented in map view (top).

The data that were collected were checked for any biases. USGS and NGL use the same GPS stations for their data, however, they process their data differently. Comparing the USGS and NGL data for the year before the Ridgecrest earthquake sequence (3 July 2018 to 3 July 2019) shows similar results. The calculated creep rate using the USGS data was 30.5 ± 2.5 mm/yr (2σ). Using the NGL data to calculate the creep rate yields 33.5 ± 2 mm/yr (2σ). Their uncertainties allow both of these calculations to overlap. However, the different results show there is some bias in how each organization processes their data.

The calculated net average magnitude changes for the USGS and NGL GPS data in the month timeseries were -7.01 ± 2.5 mm/yr (2σ) and 54.41 ± 2 mm/yr (2σ), respectively. The large value from the NGL results suggest that the reference frame of North America may have

been moved during this timeframe. Additionally, many of the GPS stations in the month timeseries (Figure 11) show orthogonal motion relative to the San Andreas Fault. This implies there was minimal components of the resultant vectors in the opposite direction of plate motion which would otherwise describe a decrease in the overall creep rate.

A few explanations can be inferred. The change in the creep rate could have been low enough to be unresolvable by the GPS equipment. Additionally, minor landslides due to the earthquake or a change in the reference frame's location (or a combination of both) could have systematically skewed the month timeseries GPS results. Lastly, the results could imply that the creep rate was unaffected by the small change in stress. The maximum calculated change of stress along the central San Andreas Fault was a decrease of 0.02 bar (at point B in Figure 14). The smallest stress change was calculated to be nearly 0 bar (at point A in Figure 14).

If the creep rate did not change, it would explain why there was no measurable net difference. This conclusion brings to light an interesting idea. There could be a theoretical critical stress value which must be achieved in order to initiate a detectable change in creep. It was highly likely that the small change in stress (maximum of 0.02 bar) was not enough to affect creep along this section of the San Andreas Fault.

A similar study completed by Meng and others (2013) observed a decrease in the creep rate of the CSAF from the $M_w$ 6.6 2003 San Simeon Earthquake. The magnitude of this earthquake was smaller than that of the mainshock from the Ridgecrest sequence. However, the epicenter was much closer to the central San Andreas Fault. Therefore, the amount of stress that was decreased along the CSAF was greater than that from the Ridgecrest sequence. Using a Coulomb stress analysis, Meng and others (2013) calculated a maximum decrease in stress of 0.08 bar along the central San Andreas Fault, four times higher than the calculated stress decrease from the Ridgecrest sequence. The decrease in creep was observed for several weeks before returning to normal background levels. The results from Meng and others (2013) show that any change in stress is only temporary. A 0.02 bar decrease would be short lived before stress quickly reaccumulates along the fault. There would not have been enough time for any significant change to be detected using GPS station data.

The theoretical critical value of stress must lie between 0.08 and 0.02 bar in order for any detectable change in creep to occur along the central San Andreas Fault.

## CONCLUSION

The significance of this study is to further understand the impact large earthquakes ($\geq M_w$ 7.0) near plate margins can have on the plate boundary. The San Andreas Fault is one of the most studied faults in the world. If large earthquakes not directly located on a plate boundary can affect the San Andreas Fault, seismologists could build better earthquake forecast models. These models could assist in predicting the likelihood of a large "unzip" event where one large earthquake causes another as a fault ruptures down its strike. It is fundamental to learn as much as possible in order to better prepare for future earthquakes.

The goal of this study was to observe any measurable change in the creep rate of the CSAF. Additionally, quantifying the stress change provided an explanation for the GPS observations. Any change in the creep rate that was associated with the 2019 Ridgecrest earthquake sequence was undetectable using my methods. For that reason, the hypothesis is rejected. This does not imply a change did not occur. However, it does imply that if there was a change in the creep rate it was lower than the uncertainty of the GPS data and thus could not be resolved to any degree of certainty.

## ACKNOWLEDGMENTS

I would like to personally thank my advisor, Dr. Mong-Han Huang, for assisting me throughout senior thesis. I deeply appreciate his

virtual meeting accommodations while I am on the other side of the country. Additionally, he provided the GMT and Matlab scripts needed to create the GPS vector plots (Figure 11) which were crucial to this study. Dr. Huang also assisted me during my Excel calculations. He would always respond to my emails before the sun would be up in California. Dr. Huang made my undergraduate experience extremely memorable and enjoyable. I cannot thank him enough. He has guided me through senior thesis and has helped shaped me into becoming a professional geologist.

In addition, I would also like to thank Dr. Philip Piccoli for providing assistance and feedback while writing the proposal and the final draft for this project. Dr. Piccoli provided edits and comments in record time which were vital to completing this research paper. I appreciate his accommodations he has made for me during senior thesis talks as I was unable to present my work in person for Geology 394 and half of Geology 393 due to Covid-19 restrictions. He was always open to discuss my progress not only in senior thesis, but also my academic career path. Dr. Piccoli was one of the first faculty members I met on campus and has left a positive impact on my life as I continue on my academic journey.

I would also like to thank to those in Dr. Huang's Active Tectonics Laboratory research group: Jacob Aisin, Kendal Grubb, Berit Hudson-Rasmussen, Shannan Jones, Kathryn Robbins, and Sophia Zipparo. Thank you all for your valuable feedback on my practice senior thesis presentations during our research meetings both in person and virtually over the last year.

Additionally, I would like to thank Dr. Wenlu Zhu for approving this project in its early stages. She approved this project even before I knew what I was getting myself into.

Also, I would like to thank Dr. Vedran Lekic for his thoughtful advice. He was happy to discuss this project even before I knew how I was going to complete it. The Matlab skills I learned from his observational geophysics class this semester came in handy for this project.

I want to acknowledge my friends who have helped me along this rewarding journey. Those in the University of Maryland Geology Club who helped organize senior thesis practice talks: Maeve Kessler, Adaire Nehring, and William Nguyen. Thank you so much for your incredibly valuable comments on my presentations! Additionally, I would like to thank my other senior thesis friends: Kendal Grubb, Caerwyn Hartten, Sam Hommel, Braden Lense, Bill Li, and Justus McMillian. I wish you all the best of luck on your thesis papers and presentations next semester. Thank you for always being there through the ups and downs on this crazy rollercoaster ride.

**APPENDICES**

## Appendix I

Description: Below is the GMT script used to create plot 1a. in Figure 11. The script is the same for all other plots, however, the magnitudes of the unit vectors much be changed depending on the timeseries or reference frame (see example below). Additionally, the output name should be updated as well. Note, the fault data file must be downloaded from the USGS website and saved in the appropriate folder. This script was provided by Dr. Mong-Han Huang.

Example

```
echo -120.47329 35.89979 **E** **N** 2.5 2.5 0 LAND | gmt psvelo -N -R -JM -W1,black ${AMP} -
G0 -O -K >> ${output}
```

**E** - magnitude of the east vector
**N** - magnitude of the north vector

--- Script begins below ---

```
#!/bin/sh

gps=1mnthCentral.txt
Fault1=Historic.txt
Fault2=Quaternary.txt
Fault3=Holocene_LatestPleistocene.txt
Fault4=Mid_LateQuaternary.txt
Fault5=LateQuaternary.txt

output=1YR_B4_Central.ps

# awk '{print $1,$2,$3,$4,0,10,10}' | $gps > pre.txt


#################################################
gmtset BASEMAP_TYPE plain
gmtset FONT_ANNOT_PRIMARY 9p FONT_TITLE 9p FONT_LABEL 9p
range=-121.4/-119.75/35.6/36.75
proj=-JM15

AMP=-Se0.1/0.95/10

#################################################
gmt pscoast -R${range} -L-120.3/36.7/36.7/50 -Df $proj -W3,0 -S250 -K -P > ${output}

gmt psxy ${Fault2} $proj -R -W.5,red -An -K -O >> ${output}
gmt psxy ${Fault3} $proj -R -W.5,red -An -K -O >> ${output}
gmt psxy ${Fault4} $proj -R -W.5,red -An -K -O >> ${output}
gmt psxy ${Fault5} $proj -R -W.5,red -An -K -O >> ${output}

echo -120.47329 35.89979 -23.941 38.595 2.5 2.5 0 LAND | gmt psvelo -N -R -JM -W1,black ${AMP} -
G0 -O -K >> ${output}
```

```
echo -120.4337 35.93935 -13.714 17.876 2.5 2.5 0 CANP | gmt psvelo -R -JM -W1,black ${AMP} -G0 -O -K >> ${output}

echo -121.18844 36.55952 -26.539 33.819 2.5 2.5 0 P247 | gmt psvelo -N -R -JM -W1,black ${AMP} -G0 -O -K >> ${output}

echo -121.06441 36.61165 -16.473 9.2768 2.5 2.5 0 P249 | gmt psvelo -R -JM -W1,black ${AMP} -G0 -O -K >> ${output}

echo -121.0509 36.30216 -25.852 36.661 2.5 2.5 0 P174 | gmt psvelo -N -R -JM -W1,black ${AMP} -G0 -O -K >> ${output}

echo -120.85306 36.51591 -11.723 14.21 2.5 2.5 0 P286 | gmt psvelo -R -JM -W1,black ${AMP} -G0 -O -K >> ${output}

echo -120.37096 35.74793 -21.839 31.564 2.5 2.5 0 P533 | gmt psvelo -R -JM -W1,black ${AMP} -G0 -O -K >> ${output}

echo -120.28526 35.80667 -12.029 19.998 2.5 2.5 0 P283 | gmt psvelo -R -JM -W1,black ${AMP} -G0 -O -K >> ${output}

echo -120.2926 35.68891 -20.749 29.214 2.5 2.5 0 P542 | gmt psvelo -N -R -JM -W1,black ${AMP} -G0 -O -K >> ${output}

echo -120.4341 35.96947 -12.636 15.965 2.5 2.5 0 MNMC | gmt psvelo -R -JM -W1,black ${AMP} -G0 -O -K >> ${output}

echo -120.22789 35.72917 -13.523 21.155 2.5 2.5 0 P602 | gmt psvelo -R -JM -W1,black ${AMP} -G0 -O -K >> ${output}


# gmt psvelo << END -R -JM -W1,black -Se0.1 -G0 -O -K >> ${output}

echo -120.2 36.5 20 0 2.5 2.5 0 20 mm/yr 95% conf. | gmt psvelo -R -JM -W1,black ${AMP} -G0 -O -K >> ${output}

gmt psbasemap -B.5f1WeNs -R $proj -O -K >> ${output}


open ${output}
```

## Appendix II

Description: USGS data spreadsheet where my calculations and data are saved. The yellow rows represent the P249 station, which is kept used as the reference station in some calculations. Rows 1 through 16 shows data for the year timeseries. Rows 17 through 31 shows data for the month timeseries. All data are in terms of mm/yr except for *lat* and *long* which are in degrees. Bottom plot shows the stations relative to P249. The uncertainty for each of the data columns (except lat/long) is ± 2 mm/yr.

| | A | B | C | D | E | F | G | H | I | J | K | L | M | N | O | P | Q | R | S |
|---|---|---|---|---|---|---|---|---|---|---|---|---|---|---|---|---|---|---|---|
| 1 | | Central San Andreas Fault | | | | | | | | | | | | | | | | | |
| 2 | Plate | Station | 1 yr before | E | N | Resultant | | 1 yr after | E | N | Resultant | | Delta MAG | | Delta N | Delta E | | lat | long |
| 3 | P | LAND | | -23.994 | 38.82 | 45.63666 | | | -22.242 | 30.03 | 37.36987 | | 8.266783 | | -8.79 | 1.752 | | 35.89979 | -120.4733 |
| 4 | NA | CANP | | -13.714 | 17.876 | 22.53054 | | | -13.863 | 20.434 | 24.69273 | | 2.162196 | | 2.558 | -0.149 | | 35.93935 | -120.4337 |
| 5 | P | P247 | | -26.539 | 33.819 | 42.98887 | | | -27.874 | 35.97 | 45.50605 | | 2.517178 | | 2.151 | -1.335 | | 36.55952 | -121.1884 |
| 6 | NA | P249 | | -16.473 | 9.2768 | 18.90552 | | | -8.5821 | 11.247 | 14.14735 | | 4.758174 | | 1.9702 | 7.8909 | | 36.61165 | -121.0644 |
| 7 | P | P174 | | -25.852 | 36.661 | 44.85928 | | | -26.539 | 36.641 | 45.24247 | | 0.383195 | | -0.02 | -0.687 | | 36.30216 | -121.0509 |
| 8 | NA | P286 | | -11.723 | 14.21 | 18.42153 | | | -9.882 | 13.878 | 17.03681 | | 1.384724 | | -0.332 | 1.841 | | 36.51591 | -120.8531 |
| 9 | P | P533 | | -21.839 | 31.564 | 38.38265 | | | -20.866 | 31.59 | 37.85919 | | 0.523465 | | 0.026 | 0.973 | | 35.74793 | -120.371 |
| 10 | NA | P283 | | -12.029 | 19.998 | 23.33703 | | | -12.274 | 21.614 | 24.85591 | | 1.518879 | | 1.616 | -0.245 | | 35.80667 | -120.2853 |
| 11 | P | P542 | | -20.749 | 29.214 | 35.83265 | | | -21.368 | 29.294 | 36.2592 | | 0.426554 | | 0.08 | -0.619 | | 35.68891 | -120.2926 |
| 12 | NA | MNMC | | -12.636 | 15.965 | 20.36049 | | | -13.152 | 18.423 | 22.63586 | | 2.275363 | | 2.458 | -0.516 | | 35.96947 | -120.4341 |
| 13 | NA | P602 | | -13.523 | 21.155 | 25.10788 | | | -15.561 | 22.376 | 27.25491 | | 2.147031 | | 1.221 | -2.038 | | 35.72917 | -120.2279 |
| 14 | | | Average | -18.09736 | 24.41444 | 30.57846 | mm/yr | | | | 30.26003 | mm/yr | 2.396686 | average change | | | | | |
| 15 | | | | | | | Net change | -0.318432 | mm/yr | | | | | | | | | | |
| 16 | | | | | | | | | | | | | | | | | | | |
| 17 | | | 1 mnth before (30 days) | | | | 1 mnth after (30 days) | | | | | | Delta MAG | | Delta N | Delta E | | | |
| 18 | P | LAND | | -37.847 | 40.879 | 55.70896 | | | -43.445 | 23.788 | 49.53117 | | 17.98443 | | -17.091 | -5.598 | | 35.89979 | -120.4733 |
| 19 | NA | CANP | | -26.079 | 27.655 | 38.01201 | | | -24.266 | 7.9014 | 25.52001 | | 19.83662 | | -19.7536 | 1.813 | | 35.93935 | -120.4337 |
| 20 | P | P247 | | -38.133 | 51.278 | 63.90273 | | | -45.814 | 37.378 | 59.1273 | | 15.88105 | | -13.9 | -7.681 | | 36.55952 | -121.1884 |
| 21 | NA | P249 | | -9.8525 | 33.532 | 34.94949 | | | -16.496 | 18.925 | 25.10525 | | 16.04682 | | -14.607 | -6.6435 | | 36.61165 | -121.0644 |
| 22 | P | P174 | | -41.123 | 38.83 | 56.55855 | | | -49.085 | 22.5 | 53.99618 | | 18.16762 | | -16.33 | -7.962 | | 36.30216 | -121.0509 |
| 23 | NA | P286 | | -47.212 | 34.987 | 58.76277 | | | -19.941 | 0.2509 | 19.94258 | | 44.16225 | | -34.7361 | 27.271 | | 36.51591 | -120.8531 |
| 24 | P | P533 | | -30.592 | 38.29 | 49.01015 | | | -47.973 | 14.057 | 49.99008 | | 29.82176 | | -24.233 | -17.381 | | 35.74793 | -120.371 |
| 25 | NA | P283 | | -28.762 | 26.125 | 38.85574 | | | -41.342 | 23.121 | 47.36815 | | 12.93369 | | -3.004 | -12.58 | | 35.80667 | -120.2853 |
| 26 | P | P542 | | -30.017 | 36.725 | 47.43149 | | | -53.938 | 18.448 | 57.00558 | | 30.1042 | | -18.277 | -23.921 | | 35.68891 | -120.2926 |
| 27 | NA | MNMC | | -29.618 | 35.752 | 46.42662 | | | -21.543 | 25.134 | 33.10315 | | 13.3397 | | -10.618 | 8.075 | | 35.96947 | -120.4341 |
| 28 | NA | P602 | | -28.477 | 16.791 | 33.05869 | | | -29.586 | 11.908 | 31.8925 | | 5.007352 | | -4.883 | -1.109 | | 35.72917 | -120.2279 |
| 29 | | | Average | | | 52.26772 | mm/yr | | | | 45.2582 | mm/yr | 20.29868 | average change | | | | | |
| 30 | | | | | | | | | | | | | | | | | | | |
| 31 | | | | | | | Net change | -7.009525 | mm/yr | | | | | | | | | | |

| T | U | V | W | X | Y | Z | AA | AB | AC | AD |
|---|---|---|---|---|---|---|---|---|---|---|
| | | | | | | | | | | |
| Net change from P249 | | Delta E | Delta N | Resultant | | Before year from P249 | | E | N | Resultant |
| | | -6.1389 | -10.7602 | 12.38822 | | | | -7.521 | 29.5432 | 30.48551 |
| | | -8.0399 | 0.5878 | 8.061358 | | | | 2.759 | 8.5992 | 9.030965 |
| | | -9.2259 | 0.1808 | 9.227671 | | | | -10.066 | 24.5422 | 26.52629 |
| | | 0 | 0 | 0 | | | | 0 | 0 | 0 |
| | | -8.5779 | -1.9902 | 8.805752 | | | | -9.379 | 27.3842 | 28.94581 |
| | | -6.0499 | -2.3022 | 6.47313 | | | | 4.75 | 4.9332 | 6.848282 |
| | | -6.9179 | -1.9442 | 7.185907 | | | | -5.366 | 22.2872 | 22.92408 |
| | | -8.1359 | -0.3542 | 8.143606 | | | | 4.444 | 10.7212 | 11.60574 |
| | | -8.5099 | -1.8902 | 8.717296 | | | | -4.276 | 19.9372 | 20.39059 |
| | | -8.4069 | 0.4878 | 8.42104 | | | | 3.837 | 6.6882 | 7.71068 |
| | | -9.9289 | -0.7492 | 9.957126 | | | | 2.95 | 11.8782 | 12.23904 |
| | | | | | | | | | | |
| | | | | | | | | | | |
| | | | | | | | | | | |
| Net change from P249 | | Delta E | Delta N | Resultant | | Before mnth from P249 | | E | N | Resultant |
| | | 1.0455 | -2.484 | 2.695056 | | | | -27.9945 | 7.347 | 28.94254 |
| | | 8.4565 | -5.1466 | 9.899489 | | | | -16.2265 | -5.877 | 17.258 |
| | | -1.0375 | 0.707 | 1.25549 | | | | -28.2805 | 17.746 | 33.38723 |
| | | 0 | 0 | 0 | | | | 0 | 0 | 0 |
| | | -1.3185 | -1.723 | 2.169602 | | | | -31.2705 | 5.298 | 31.71613 |
| | | 33.9145 | -20.1291 | 39.43823 | | | | -37.3595 | 1.455 | 37.38782 |
| | | -10.7375 | -9.626 | 14.4206 | | | | -20.7395 | 4.758 | 21.27829 |
| | | -5.9365 | 11.603 | 13.03348 | | | | -18.9095 | -7.407 | 20.30844 |
| | | -17.2775 | -3.67 | 17.66298 | | | | -20.1645 | 3.193 | 20.41574 |
| | | 14.7185 | 3.989 | 15.24947 | | | | -19.7655 | 2.22 | 19.88978 |
| | | 5.5345 | 9.724 | 11.18869 | | | | -18.6245 | -16.741 | 25.04263 |
| | | | | | | | | | | |

# Appendix III

Description: NGL data spreadsheet where my calculations and data are saved. The yellow rows represent the P249 station. Rows 1 through 16 shows data for the year timeseries. Rows 17 through 32 shows data for the month timeseries. All data are in terms of mm/yr except for *lat* and *long* which are in degrees. The uncertainty for each of the data columns (except lat/long) is ± 2 mm/yr.

| | A | B | C | D | E | F | G | H | I | J | K | L | M | N | O | P | Q | R | S |
|---|---|---|---|---|---|---|---|---|---|---|---|---|---|---|---|---|---|---|---|
| 1 | | Central San Andreas Fault | | | | | | | | | | | | | | | | | |
| 2 | Plate | Station | 1 yr before | E | N | Resultant | | 1 yr after | E | N | Resultant | | Delta MAG | | Delta N | Delta E | | lat | long |
| 3 | P | LAND | | -24.172 | 42.124 | 48.566624 | | | -23.466 | 30.996 | 38.876795 | | -9.689829 | | -11.128 | 0.706 | | 35.89979 | -120.4733 |
| 4 | NA | CAND | | -13.737 | 21.272 | 25.32199 | | | -15.821 | 21.219 | 26.467905 | | 1.1459156 | | -0.053 | -2.084 | | 35.93935 | -120.4337 |
| 5 | P | P247 | | -26.54 | 37.259 | 45.744996 | | | -28.968 | 36.953 | 46.953905 | | 1.2089092 | | -0.306 | -2.428 | | 36.55952 | -121.1884 |
| 6 | NA | P249 | | -16.533 | 12.746 | 20.875838 | | | -9.8114 | 12.156 | 15.621521 | | -5.254317 | | -0.59 | 6.7216 | | 36.61165 | -121.0644 |
| 7 | P | P174 | | -25.913 | 40.083 | 47.729765 | | | -27.826 | 37.505 | 46.700228 | | -1.029537 | | -2.578 | -1.913 | | 36.30216 | -121.0509 |
| 8 | NA | P286 | | -12.64 | 18.554 | 22.450401 | | | -10.944 | 14.961 | 18.536522 | | -3.913879 | | -3.593 | 1.696 | | 36.51591 | -120.8531 |
| 9 | P | P553 | | -21.962 | 35.095 | 41.400344 | | | -22.109 | 32.524 | 39.32707 | | -2.073274 | | -2.571 | -0.147 | | 35.74793 | -120.371 |
| 10 | NA | P283 | | -12.046 | 23.408 | 26.325664 | | | -13.63 | 23.037 | 26.767149 | | 0.4414852 | | -0.371 | -1.584 | | 35.80667 | -120.2853 |
| 11 | P | P542 | | -20.738 | 32.639 | 38.670001 | | | -22.492 | 30.173 | 37.633761 | | -1.036239 | | -2.466 | -1.754 | | 35.68891 | -120.2926 |
| 12 | NA | MNMC | | -12.651 | 19.245 | 23.030802 | | | -14.225 | 19.362 | 24.025771 | | 0.9949693 | | 0.117 | -1.574 | | 35.96947 | -120.4341 |
| 13 | NA | P602 | | -13.588 | 24.614 | 28.115525 | | | -16.659 | 23.392 | 28.717729 | | 0.6022039 | | -1.222 | -3.071 | | 35.72917 | -120.2279 |
| 14 | | | Average Creep | -18.22909 | 27.912636 | 33.475632 | mm/yr | | -18.72285 | 25.661636 | 31.784396 | mm/yr | -1.691236 | | -2.251 | -0.493764 | | | |
| 15 | | | | | | | | | | | | | | | | | | | |
| 16 | | | | Net change | -1.691236 | mm/yr | | | | | | | | | | | | | |
| 17 | | Central San Andreas Fault | | | | | | | | | | | | | | | | | |
| 18 | Plate | Station | 1 mnth before | E | N | Resultant | | 1 mnth after | E | N | Resultant | | Delta MAG | | Delta N | Delta E | | lat | long |
| 19 | P | LAND | | -11.206 | 35.399 | 37.13036 | | | -81.408 | 26.608 | 85.646063 | | 48.515703 | | -8.791 | -70.202 | | 35.89979 | -120.4733 |
| 20 | NA | CAND | | -3.0306 | 18.061 | 18.313499 | | | -65.699 | 11.593 | 66.713988 | | 48.400489 | | -6.468 | -62.6684 | | 35.93935 | -120.4337 |
| 21 | P | P247 | | -11.362 | 47.494 | 48.834159 | | | -90.496 | 39.657 | 98.803865 | | 49.969706 | | -7.837 | -79.134 | | 36.55952 | -121.1884 |
| 22 | NA | P249 | | 15.642 | 30.554 | 34.325196 | | | -57.6 | 22.972 | 62.011876 | | 27.68668 | | -7.582 | -73.242 | | 36.61165 | -121.0644 |
| 23 | P | P174 | | -14.782 | 29.944 | 33.393872 | | | -96.272 | 21.345 | 98.609873 | | 65.216001 | | -8.599 | -81.49 | | 36.30216 | -121.0509 |
| 24 | NA | P286 | | 2.5798 | 3.595 | 4.4248608 | | | -64.801 | 10.74 | 65.684985 | | 61.260124 | | 7.145 | -67.3808 | | 36.51591 | -120.8531 |
| 25 | P | P553 | | -7.7113 | 30.482 | 31.442272 | | | -89.233 | 20.238 | 91.499207 | | 60.056935 | | -10.244 | -81.5217 | | 35.74793 | -120.371 |
| 26 | NA | P283 | | -4.7469 | 18.973 | 19.557806 | | | -83.465 | 26.421 | 87.54699 | | 67.989184 | | 7.448 | -78.7181 | | 35.80667 | -120.2853 |
| 27 | P | P542 | | -2.4398 | 29.591 | 29.691411 | | | -93.975 | 25.719 | 97.430835 | | 67.739424 | | -3.872 | -91.5352 | | 35.68891 | -120.2926 |
| 28 | NA | MNMC | | -0.6199 | 29.423 | 29.429529 | | | -62.459 | 25.433 | 67.438596 | | 38.009066 | | -3.99 | -61.8391 | | 35.96947 | -120.4341 |
| 29 | NA | P602 | | 0.5774 | 14.122 | 14.133799 | | | -76.196 | 15.591 | 77.774737 | | 63.640938 | | 1.469 | -76.7734 | | 35.72917 | -120.2279 |
| 30 | | | Average Creep | -3.372664 | 26.148909 | 27.334251 | mm/yr | | -78.32764 | 22.392455 | 81.74191 | mm/yr | 54.407659 | | -3.756455 | -74.95497 | | | |
| 31 | | | | | | | | | | | | | | | | | | | |
| 32 | | | | Net change | 54.407659 | mm/yr | | | | | | | | | | | | | |

## Appendix IV

Description: The Matlab script that is used to create the right creepmeter plot in Figure 15. The code is the same for all other creepmeter plots except the data file (D) needs to be changed. In addition, the title, xlabel, and ylabel need to be updated for other plots. The creepmeter data is directly downloaded from USGS as an zipped file. Once the file has been unzipped, a plot can be created using this script. This script was provided by Dr. Mong-Han Huang. Comment lines are indicated by the percent symbol (`%`) and are not part of the script. Instead, they are meant as a guide. Additional Creepmeter plots can be found in Appendix VI.

--- Script begins below ---

```
D = load('xmd1.10min'); % Loads creepmeter data downloaded from USGS

X = D(:,2); % Decimal Date in UTC
Y = D(:,3); % Displacement Data in mm/10 mins

year = D(:,1);
X(year~=2019)=[]; % Finds data from 2019
Y(year~=2019)=[]; % Finds data from 2019

figure(1)
plot(X,Y);
title('Middle Ridge (XMD1)');
xlabel('Decimal Day');
ylabel('Displacement (mm)');

xlim([178.6 194.2]);
% Zooms in to 7 days before and after the earthquake sequence
% Foreshock occurred at 185.7 UTC
% Mainshock occurred at 187.1 UTC
```

## **Appendix V**

University of Maryland Honor Code

I pledge on my honor that I have not given or received any unauthorized assistance or plagiarized on this assignment

Adam Margolis

30 November 2020

## REFERENCES


Arizona State University (2018). 'Slow earthquakes' on San Andreas Fault increase risk large quakes, say ASU geophysicists. https://asunow.asu.edu/2018018-discoveries-asu-geophysicists-say-slow-earthquakes-san-andreas-fault-increase-risk-large-quakes. Accessed 7 April 2020.

Bilham, R.; Castillo, B. (2020). The July 2019 Ridgecrest, California Earthquake Sequence Recorded by Creepmeters: Negligible Epicentral Afterslip and Prolonged Triggered Slip at Teleseismic Distances. *Bulletin of the Seismological Society of America*, 91(2A), 707-720. doi:10.1785/0220190293.

Blewitt, G.; Hammond, W.C.; Kreemer, C. (2018). Harnessing the GPS Data Explosion for Interdisciplinary Science. *Science News by AGU*.

Harris, R.A. (2017). Large earthquakes and creeping faults. *Reviews of Geophysics*, 55, 169-198. doi:10.1002/2016RG000539.

Hussain, E.; Wright, T.J.; Walters, R.J.; Bekaert, D.; Hooper, A.; Houseman, G.A. (2016). Geodetic observations of posteismic creep in the decade after the 1999 Izmit earthquake, Turkey: Implications for a shallow slip deficit. *Journal of Geophysical Research – Solid Earth*, 121(4), 2980-3001. doi:10.1002/2015JB012737.

Ikari, M.J. (2019). Laboratory Slow Slip Events in Natural Geological Materials. *Geophysical Journal International,* 218(1), 354-387. doi:10.1093/gji/ggz143.

Kaduri, M.; Gratier, J.P.; Renard, F.; Çakir, Z.; Lasserre, C. (2017). The implications of fault zone transformation on aseismic creep: Example of the North Anatolian Fault, Turkey. *Journal of Geophysical Research – Solid Earth*, 122(6), 4208-4236. doi: 10.1002/2016JB013803.

Kalkan, E. (2001). Attenuation relationship based on strong motion data recorded in Turkey. *The Graduate School of Natural and Applied Sciences of The Middle East Technical University.* M.S. Dissertation, Turkey.

Kim, A.; Dreger, D.S. (2008). Rupture process of the 2004 Parkfield earthquake from near-fault seismic waveform and geodetic records. *Journal of Geophysical Research – Solid Earth*, 113(B7). doi:10.1029/2007JB005115.

Lee, J.C.; Jeng, F.S.; Chu, H.T.; Angelier, J.; Hu, J.C. (2000). A rod-type creepmeter for measurement of displacement in active fault zone. *Earth Planets Space*, 52, 321-328.

Mahmud, T.; Hayat, T.; Haque, D.M.E. (2019). Three Dimensional Surface Displacement Measurement of Ridgecrest Earthquake: A Multi-Sensor Approach Incorporating InSAR and Optical Image Sub-pixel Correlation. *American Geophysical Union*. *Fall Meeting abstracts,* #S31F-0463.

Mallman, E.P.; Zoback, M.D. (2007). Assessing elastic Coulomb stress transfer models using seismicity rates in southern California and southwestern Japan. *Journal of Geophysical Research – Solid Earth*, 112(B3), 1-21. doi:10.1029/2005/JB004076.

McGill, S.; Dergham, S.; Barton, K.; Berney-Ficklin, T.; Grant, D.; Hartling, C.; Hobart, K.; Minnich, R.; Rodriguez, M.; Runnerstorm, E.; Russell, J.; Schmoker, K.; Stumfall, M.; Townsend, J.; Williams, J. (2002). Paleoseismology of the San Andreas Fault at Plunge Creek, near San Bernardino,

Southern California. *Bulletin of the Seismological Society of America*, 92(7), 2803-2840. doi: 10.1785/0120000607.

Meng, X.; Peng, Z.; Hardeback, J.L. (2013). Seismicity around Parkfield correlates with static shear stress changes following the 2003 Mw6.5 San Simeon earthquake. *Journal of Geophysical Research – Solid Earth*, 118(7), 3576-3591. doi: 10.1002/jgrb.50271.

Milner, K.R.; Field, E.H.; Sarvran, W.H.; Jordan, T.H.; Page, M.; Wener, M.J. (2019). Operational earthquake forecasting during the M6.4 Searles Valley and M7.1 Ridgecrest sequence using the UCEF3-ETAS model-evaluation and lessons. *American Geophysical Union*. *Fall Meeting abstracts,* #S31G-0510.

Ross, Z.E.; Idini, B.; Jia, Z.; Stephenson, O.L.; Zhong, M.; Wang, X.; Zhan, Z.; Simons, M.; Fielding, E.J.; Yun, S.; Hauksson, E.; Moore, A.W.; Lui, Z.; Jung, J. (2019). Hierarchical Interlocked Orthogonal Faulting in the 2019 Ridgecrest Earthquake Sequence. *Science*, 366(6463), 346-351. doi:10.1126/science.aaz0109.

Shirzaei, M.; Bürgmann, R. (2013). Time-dependent model of creep on the Hayward fault from joint inversion of 18 years of InSAR and surface creep data. *Journal of Geophysical Research – Solid Earth*, 118(4), 1733-1746. doi:10.1002/jgrb.50149.

Smith, B.; Sandwell, D. (2003). Coulomb stress accumulation along the San Andreas Fault system. *Journal of Geophysical Research – Solid Earth*, 108(B6). doi:10.1029/2002JB002136.

Titus, S.J.; DeMets, C.; Tikoff, B. (2006). Thirty-Five-Year Creep Rates for the Creeping Segment of the San Andreas Fault and the Effects of the 2004 Parkfield Earthquake: Constraints from Alignment Arrays, Continuous Global Positioning System, and Creepmeters. *Bulleting of the Seimological Society of America*. 96(4B), S250-S268. doi:10.1785/0120050811.

Toda, S.; Stein, R. (2019). Ridgecrest Earthquake Shut Down Cross-Fault Aftershocks, *Temblor*. doi:10.32858/temblor.043.

United States Geological Survey (1999). Farallon Plate. https://pubs.usgs.gov/gip/dynamic/Farallon.html. Accessed 7 April 2020.

United States Geological Survey (2019). M 7.1 – 2019 Ridgecrest Earthquake Sequence. https://earthquake.usgs.gov/earthquakes/eventpage/ci38457511/executive. Accessed 13 November 2020.

United States Geological Survey (2020). CentralCalifornia Network https://earthquake.usgs.gov/monitoring/gps/CentralCalifornia. Accessed 13 November 2020.